

Anomalous Hall effect in an antiferromagnetic CeGaSi single crystal


Jing Gong ^{1,2}, Huan Wang,^{1,2} Kun Han,^{1,2} Xiang-Yu Zeng,^{1,2} Xiao-Ping Ma,^{1,2} Yi-Ting Wang,^{1,2} Jun-Fa Lin,^{1,2} Xiao-Yan Wang,^{1,2} and Tian-Long Xia ^{1,2,3,4,*}

¹Department of Physics, Renmin University of China, Beijing 100872, China

²Beijing Key Laboratory of Opto-electronic Functional Materials & Micro-nano Devices, Renmin University of China, Beijing 100872, China

³Key Laboratory of Quantum State Construction and Manipulation (Ministry of Education), Renmin University of China, Beijing 100872, China

⁴Laboratory for Neutron Scattering, Renmin University of China, Beijing 100872, China

 (Received 11 July 2023; revised 11 December 2023; accepted 11 January 2024; published 26 January 2024)

We report a detailed investigation of the magnetic and electrical transport properties in an antiferromagnetic CeGaSi crystal. It orders ferromagnetically within the ab plane and antiferromagnetically along the c axis below T_N (~ 12 K). The magnetotransport in CeGaSi shows anisotropy with the emergence of negative magnetoresistance (MR) within the ab plane and along the c axis. At low temperatures, the initially negative MR within the ab plane changes sign and becomes positive with B further increasing and approaching saturation. When the field is applied along the c axis, the MR remains negative, as a result of the suppression of spin scattering in the antiferromagnetic state. Interestingly, different Hall responses are also demonstrated. A prominent anomalous Hall effect (AHE) is observed with $B \parallel ab$ in CeGaSi with a maximum value of anomalous Hall conductivity $|\sigma_{xz}^A| \sim 128 \Omega^{-1} \text{cm}^{-1}$. The scaling behaviors of anomalous Hall resistivity and conductivity indicate the skew scattering as the dominant mechanism of AHE in CeGaSi. However, the AHE is absent and only the normal Hall effect is observed with $B \parallel c$. These fascinating findings in MR and Hall measurements not only establish CeGaSi as a new platform to study AHE, but also deepen our understanding on the interesting physical phenomena associated with magnetic properties.

DOI: [10.1103/PhysRevB.109.024434](https://doi.org/10.1103/PhysRevB.109.024434)

I. INTRODUCTION

The anomalous Hall effect (AHE) has been an enduring topic ever since it was discovered a century ago [1,2], and it has attracted significant interest due to its highly tunable physical properties and great potential in spintronic device applications [3–7]. Building on results from experiment and theory, the AHE in ferromagnetic (FM) systems [8] is proposed to be proportional to spontaneous magnetization M . It is well established that three possible mechanisms are responsible for AHE. The intrinsic Karplus-Luttinger (K-L) mechanism is related to the band structure of ferromagnetic conductors with spin-orbit coupling (SOC), which has been interpreted as a manifestation of Berry curvature in momentum space (intrinsic mechanism) [8–13]. It presents the power law relation with the resistivity $\rho_{xy} \propto \rho_{xx}^2$, which has been observed in Co_2MnAl [14], Co_2MnGa [15], $\text{Co}_3\text{Sn}_2\text{S}_2$ [16,17], Fe_3GeTe_2 [18,19], and Fe_3Sn_2 [20], among others. Extrinsic mechanisms including skew scattering and the side jump are viewed as the product of impurity scattering which is also affected by SOC [21–23], yielding the relations $\rho_{xy} \propto \rho_{xx}$ or $\rho_{xy} \propto \rho_{xx}^2$, respectively, which are exhibited in the materials like KV_3Sb_5 [24], Cr_5Te_8 [25,26], and FeCr_2Te_4 [27].

Recently, AHE has been reported in the LnAlSi ($\text{Ln} = \text{Ce}, \text{Pr}$) crystal family [28–31]. In the ferromagnet $\text{PrAlGe}_{1-x}\text{Si}_x$, the mechanism responsible for the AHE inside the samples

changes from intrinsic to extrinsic by changing the ratio of Ge to Si from $x = 0$ to $x = 1$ [29]. Besides, the magnetic and electrical transport properties of the CeAlSi single crystal with noncollinear FM order was reported [30]. Interestingly, different Hall responses were found by applying the magnetic field to the easy and hard magnetization axes, respectively. In addition, the LnAlSi ($\text{Ln} = \text{La}, \text{Ce}, \text{Pr}, \text{Nd}, \text{Sm}$) crystal family [28–41] is a new class of Weyl semimetals presenting topological characteristics and abundant magnetic properties, which provides an ideal platform for the study of unique transport properties, such as quantum oscillations [28–30,33,35,36,38–41], the anomalous Nernst effect [31,32], anomalous Hall effect [28–31], and topological Hall effect [39]. These fascinating physical features inspired us to extend the investigation from the LnAlSi to LnGaSi family, which provides a stronger SOC effect that may benefit for the observation of AHE [8]. As an example, the unique physical properties in CeGaSi are explored as a first attempt.

In this paper, we have investigated the magnetic and electrical transport properties of CeGaSi, which orders ferromagnetically within the ab plane and antiferromagnetically along the c axis below T_N (~ 12 K). Specific heat measurements indicate a doublet ground state due to the crystalline electric field (CEF). Negative magnetoresistance (MR) resulting from spin-scattering suppression is observed with both $B \parallel ab$ and $B \parallel c$ configurations at low temperature. A prominent AHE is expected to be observed in CeGaSi with $B \parallel ab$, and the mechanism is quantitatively analyzed according to the framework proposed for the analysis of AHE in ferromagnetic

*tlxia@ruc.edu.cn

materials. The scaling behaviors of anomalous Hall resistivity and conductivity reveal the major contribution of skew scattering in the observed AHE; meanwhile, the side-jump and intrinsic mechanism also play an important role.

II. EXPERIMENT

Single crystals of CeGaSi and LaGaSi were grown by the self-flux method. A Ce/La ingot, Ga ingot, and Si powder with a ratio of Ce/La:Ga:Si = 1:7:2 were put into a corundum crucible and sealed in a quartz tube. The quartz tube was placed in a box furnace, which is heated to 1150 °C with 60 °C/h, and held for 12 h. Then, it was cooled to 600 °C with a rate of 3 °C/h, at which the excess Ga flux was separated from the crystals by centrifugation. The atomic proportions of CeGaSi and LaGaSi were checked to be Ce/La:Ga:Si = 1:1:1 using energy-dispersive x-ray spectroscopy (EDS; Oxford X-Max 50). The single crystal and powder x-ray diffraction (XRD) of CeGaSi were collected from a Bruker AXS D8 Advance diffractometer using Cu K_{α} radiation at 40 kV and 40 mA with 2θ ranging from 15° to 90°, a step of 0.02°, and a counting time of 2 s/step. Jana2021 was employed for the refinement. The magnetic properties were measured with a Quantum Design magnetic property measurement system (QD MPMS-3). The resistivity, specific heat, and Hall effect were measured in a Quantum Design physical property measurement system (QD PPMS-14T). Resistivity, magnetoresistance, and Hall resistivity measurement were performed by the six-probe method. The size of the investigated samples is $1.22 \times 0.43 \times 0.17 \text{ mm}^3$ and the demagnetization factor N_d is 0.63618 when the field is applied within the ab plane. The size of the investigated samples with field applied along the c axis is $1.83 \times 0.73 \times 0.15 \text{ mm}^3$ and the demagnetization factor N_d is 0.75098. To eliminate the influence from voltage probe misalignment, the raw resistivity data were evaluated by the formula $\rho_{xx}(B) = [\rho_{xx}(-7 \text{ T} \sim 7 \text{ T}) + \rho_{xx}(7 \text{ T} \sim -7 \text{ T})]/2$, $\rho_{xz}(B) = [\rho_{xz}(-7 \text{ T} \sim 7 \text{ T}) - \rho_{xz}(7 \text{ T} \sim -7 \text{ T})]/2$.

III. RESULTS AND DISCUSSION

A. Crystal structure and resistivity

As shown in Fig. 1(a), the LaPtSi-type crystal structure with space group $I4_1md$ (No. 109) is exhibited, in which Ce, Ga, and Si layers are stacked along the c axis with each layer containing only one type of element. Figure 1(b) presents the single-crystal XRD for CeGaSi, which reveals the surface of the sample as a (00 l) plane, as shown in the inset of Fig. 1(b). The powder XRD pattern for the CeGaSi is displayed in Fig. 1(c), which shows no trace of any other impurity phase but a little flux Ga. A refinement of the powder XRD pattern with the space group $I4_1md$ was performed. The obtained lattice parameters are $a = b = 4.2434 \text{ \AA}$, and $c = 14.3288 \text{ \AA}$. The longitudinal resistivity (ρ_{xx}) as a function of temperature is shown in Fig. 1(d), which increases with decreasing temperature from 300 K to 12 K, showing a semiconductor-like behavior. ρ_{xx} presents a broad hump around 60 K, which is developed by the crystalline electric field expected for the localized f states of Ce [42,43]. It can be seen that the re-

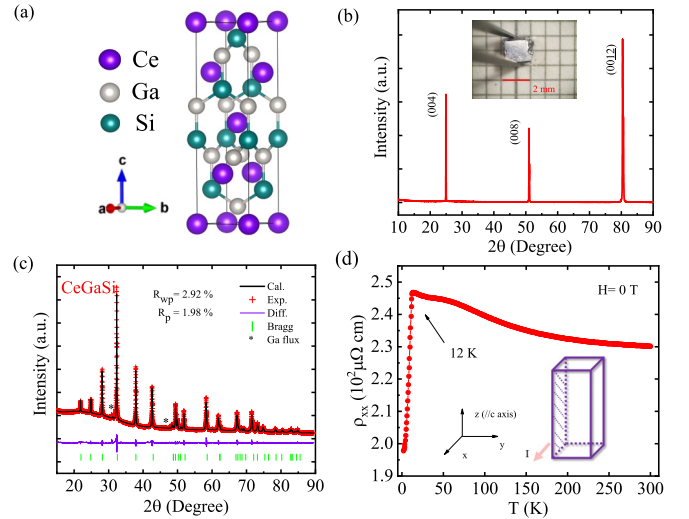


FIG. 1. (a) Crystal structure of noncentrosymmetric CeGaSi with space group $I4_1md$ (No. 109). (b) Single-crystal XRD pattern of the (00 l) plane. Inset: Picture of the polished crystal. (c) The x-ray powder-diffraction pattern of CeGaSi. The value of R_{wp} is 2.92% and R_p is 1.98%. (d) Temperature dependence of the resistivity ρ_{xx} . The inset illustrates the definition of a Cartesian coordinate system based on the tetragonal lattice.

sistivity shows a steep drop at 12 K, indicating the emergence of possible magnetic phase transition.

B. Specific heat

The specific heat of CeGaSi and nonmagnetic isostructural LaGaSi are carried out under zero magnetic field as shown in Fig. 2(a). The specific heat attains the value of $64.16 \text{ J mol}^{-1} \text{ K}^{-1}$ at 200 K, which is close to the expected Dulong-Petit limiting [44,45] value of $C_v = 3nR = 74.83 \text{ J mol}^{-1} \text{ K}^{-1}$, where $R = 8.31 \text{ J mol}^{-1} \text{ K}^{-1}$ is the gas constant and n is the atomic number of ions per formula in the material, which equals 3 in CeGaSi. As the temperature decreases, a peak around 12 K is observed, which is considered as the onset of magnetic transition and also evidenced in temperature-dependent resistivity $\rho_{xx}(T)$ [Fig. 1(d)]. The specific heat of LaGaSi does not show any anomaly, and its temperature dependence is typical for a nonmagnetic reference compound. The low-temperature region of the specific heat is enlarged for clarity as displayed in the inset of Fig. 2(a).

The magnetic contribution of CeGaSi to specific heat C_m was calculated by subtracting the specific heat of isostructural nonmagnetic LaGaSi, as shown in Fig. 2(b), in which a sharp peak at T_N and a broad hump around 70 K are respectively observed. The high-temperature hump around 70 K is related to the Schottky anomaly contributed by the CEF splitting of Ce^{3+} atomic levels, and such behavior is frequently seen in lanthanide compounds such as CeAlSi [30], NdAlSi [35,36], and SmAlSi [39]. The sharp peak around $T_N \sim 12 \text{ K}$ is due to the magnetic phase transition. In the tetragonal point symmetry of CeGaSi, the Ce^{3+} six multiplet splits into a doublet ground state and a quadruplet excited state [30]. To examine the energy spectrum of the CEF states, the magnetic entropy S_m is calculated by $S_m(T) = \int_0^T \frac{C_m(T)}{T} dT$ as plotted in

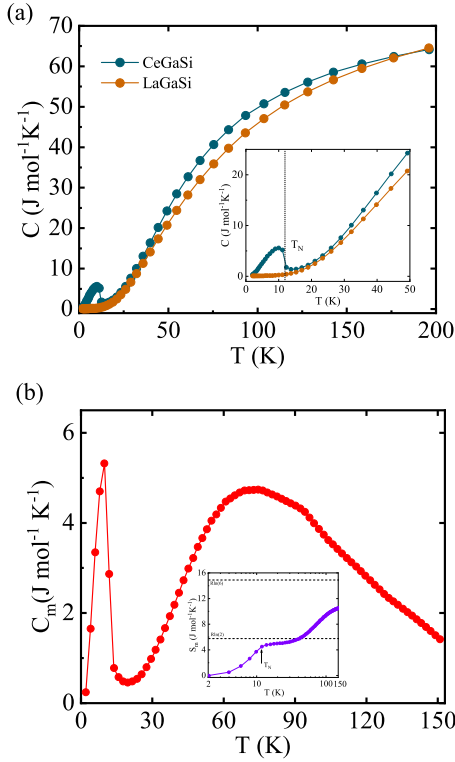


FIG. 2. (a) Temperature dependence of the specific heat in CeGaSi and LaGaSi crystals. The inset shows the low-temperature part. (b) Magnetic specific heat C_m , derived from $C_{Ce} - C_{La}$. Inset: Magnetic entropy S_m , obtained by integrating C_m/T with respect to T ; the two horizontal dashed lines stand for $R \ln(2)$ and $R \ln(6)$, respectively.

the inset of Fig. 2(b). S_m reaches a plateau with the value of $4.49 \text{ J mol}^{-1} \text{K}^{-1}$ around T_N , close to $R \ln(2)$ ($5.76 \text{ J mol}^{-1} \text{K}^{-1}$) associated with the magnetic doublet ground state, which is similar to CeAlSi [30]. At high temperature above 100 K, the reduced value of $S_m(T)$ compared with $R \ln(6)$ [30] may be attributed to the inaccurate estimate of the lattice contribution to the specific heat [46,47].

C. Magnetic properties

Figure 3(a) shows the temperature-dependent magnetic susceptibilities $\chi(T)$ with applied magnetic field $H \parallel ab$ and $H \parallel c$ under the zero-field-cooled (ZFC) and field-cooled (FC) modes. The magnitude of $\chi_{\parallel ab}$ is almost the same as that of $\chi_{\parallel c}$ at high temperature, but is about 38 times larger at 2 K, indicating the strong magnetic anisotropy. With $H \parallel ab$, as the temperature decreases, there is a sharp increase around 12 K both in ZFC and FC curves, which marks the onset of magnetic order that determines the Néel temperature. As the temperature further decreases, ZFC and FC curves begin to bifurcate. With $H \parallel c$, the ZFC and FC curves nearly saturate at low temperature with slight bifurcation. Figure 3(b) shows the inverse magnetic susceptibility $1/\chi$ curve fitted by the modified Curie-Weiss law expression between $T = 50$ K and 300 K:

$$\chi(T) = \chi_0 + \frac{C}{T - \theta}, \quad (1)$$

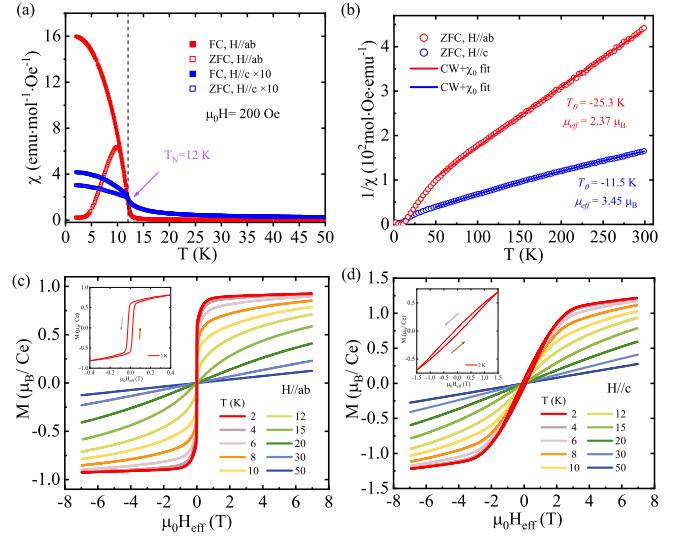


FIG. 3. (a) Low-temperature dependence of the magnetic susceptibility $\chi(T)$ in CeGaSi with $H \parallel ab$ and $H \parallel c$ for ZFC and FC and $\mu_0 H = 200$ Oe. (b) Temperature dependence of inverse magnetic susceptibility in CeGaSi from 50 K to 300 K. (c) and (d) Field-dependent magnetization $M(H)$ at different temperature for $H \parallel ab$ and $H \parallel c$, respectively. Inset: An enlarged view $M(H)$ at $T = 2$ K in low magnetic field region.

where χ_0 is the temperature-independent term including the contribution from the core diamagnetism and the Van Vleck paramagnetism, C is the Curie constant, and θ is the Weiss temperature. From the fitting of Eq. (1), the negative value of $\theta \sim -25.3$ K with $H \parallel ab$ and -11.5 K with $H \parallel c$ are obtained, respectively, which indicates the dominant AFM interaction in the paramagnetic state. The C is $0.7 \text{ emu K mol}^{-1} \text{Oe}^{-1}$ ($H \parallel ab$) and $1.49 \text{ emu K mol}^{-1} \text{Oe}^{-1}$ ($H \parallel c$). The effective magnetic moments along different directions are estimated with the relation $\mu_{\text{eff}} = \sqrt{8C}$. The yielding effective magnetic moment with $H \parallel ab$ is $2.37 \mu_B$, which approaches to the theoretical value of the free Ce^{3+} ion $\sim 2.54 \mu_B$. With $H \parallel c$, the effective magnetic moment is determined to be $3.45 \mu_B$, which is slightly larger than the value for the free Ce^{3+} ion. This excess moment may be ascribed to the spin polarization of the conduction electron [48,49].

Isothermal $M(H)$ curves in the CeGaSi single crystal with H applied parallel to the ab plane ($H \parallel ab$) and along the c axis ($H \parallel c$) are respectively shown in Figs. 3(c) and 3(d). Here $\mu_0 H_{\text{eff}} = \mu_0(H - N_d M)$, where N_d is the demagnetization factor, μ_0 is the vacuum permeability, and M is the magnetization. As shown in Figs. 3(c) and 3(d), the magnetization curves are linear at high temperatures above T_N , which corresponds to the paramagnetic state. With the temperature decreasing, the moments with $H \parallel ab$ gradually increase and a small hysteresis loop appears around zero field. At the lowest temperature 2 K, the magnetization exhibits a continuous increase until the saturation field is reached around 1.5 T ($M_S \sim 0.9 \mu_B/\text{Ce}$) with $H \parallel ab$. The saturated moment of the Ce^{3+} ion in CeGaSi is $0.9 \mu_B$, which is much smaller than the value of the free Ce^{3+} ion. This reduction in the magnetization may be attributed to the CEF [43,50]. With $H \parallel c$, as

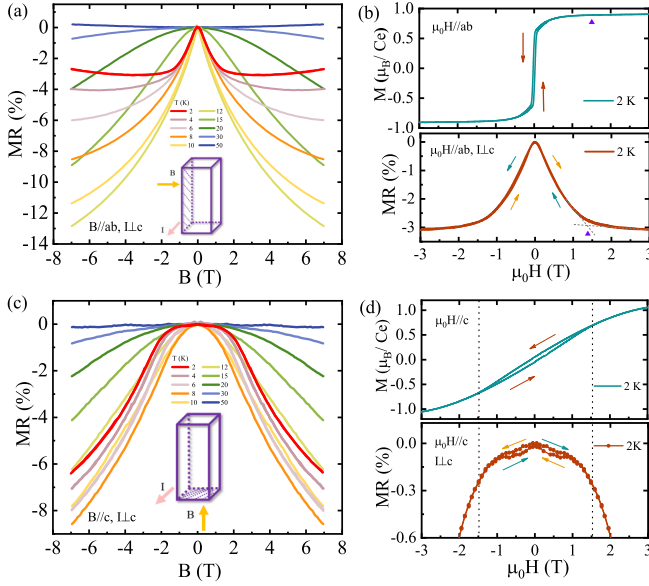


FIG. 4. Field dependence of MR in CeGaSi single crystal with $B \parallel ab$ (a) and (c) $B \parallel c$. (b) and (d) An enlarged view of $M(H)$ and MR at 2 K in low magnetic field region. The purple triangle symbols mark the transition position, the gray dashed lines are guides to the eyes, and the black dotted line marks the range where the hysteresis loop exists.

the temperature decreases below $T_N \sim 12$ K, the $M(H)$ curve presents a smooth increase as the field increases. At 2 K, a narrow hysteresis loop appears within ± 1.5 T as illustrated in the inset of Fig. 3(d) and the magnetization does not reach saturation until 7 T, which is also reflected by the negative MR and further discussed below.

D. Magnetoresistance

To investigate the anisotropic magnetotransport of CeGaSi, the field-dependent MRs with different configurations are measured with $B \parallel ab$ and $B \parallel c$, respectively, as shown in Figs. 4(a) and 4(c), in which the MR is defined as $[\rho_{xx}(B) - \rho_{xx}(0)]/\rho_{xx}(0)$. Here, $B = \mu_0(H_{\text{eff}} + M) = \mu_0[H + (1 - N_d)M]$. With $B \parallel ab$, a small positive MR at 50 K is observed, which is due to the scattering of the conduction electrons in the cyclotron motion of the carriers influenced by the Lorentz force in the magnetic field [51]. As the temperature decreases, a small negative MR is observed which may originate from a different mechanism, i.e., a chiral anomaly [52–54], electron-magnon scattering [55–57], or spin scattering [58,59]. The chiral anomaly mechanism is excluded from the experiments since negative MR also exists even when the current I is perpendicular to the field B . The electron-magnon scattering mechanism does describe the low-temperature resistivity as well as electron-electron scattering does while the data under magnetic field cannot be well fitted employing the electron-magnon mechanism. From 30 K to 12 K, the CeGaSi is in a disordered paramagnetic state at zero field. An applied field, by quenching the spin disorder, suppresses the scattering and leads to the negative MR [60–65]. Decreasing the temperature promotes the spins to be aligned with B , leading to an overall increase in the magnitude of the

negative MR, which reaches a maximum value of $\sim -13\%$ at the critical temperature 12 K [60–62]. Below $T_N \sim 12$ K, the ferromagnetic order is formed and the negative MR is weakened. At the lowest temperature 2 K, the number of magnetic domains decreases as the magnetization gradually increases along the external field, resulting in a prominent negative MR due to the suppressed scattering between electrons and magnetic domain walls. As the field increases, the spins are fully polarized along B around ~ 1.5 T, as marked with purple triangle symbol in Fig. 4(b), and the effect generated by the magnetism on MR diminishes. Accordingly, the positive orbital MR dominates, corresponding to the increase of MR above 2.5 T. The transition is marked with a purple triangle symbol in the MR curve, which is consistent with the behavior of $M(H)$ in the upper panel of Fig. 4(b).

The magnetic field dependence of MR with $B \parallel c$ at various temperatures is shown in Fig. 4(c). At 2 K, there exists a loop within ± 1.5 T marked by the black dotted line as shown in the lower panel of Fig. 4(d), consistent with the hysteresis loop at low field in the magnetization as shown in the upper panel of Fig. 4(d). Different from the clear sharp transition from negative to positive MR with $B \parallel ab$ at low temperatures, the MR with $B \parallel c$ remains negative, which is attributed to the field-induced suppression of spin scattering between conducting electrons and local magnetic moments. This negative MR indicates the magnetic moments when $B \parallel c$ cannot be easily saturated, which is in agreement with the behavior of $M(H)$ [Fig. 3(d)].

E. Hall effect

The Hall resistivities are also conducted with different configurations to reveal the anisotropic magnetotransport properties, as shown in Figs. 5(a) and 5(f). The similarity between $M(H)$ [Fig. 3(c)] and $\rho_{xz}(B)$ [Fig. 5(a)] indicates the presence of the anomalous Hall effect in CeGaSi. Commonly, the total Hall resistivity ρ_{xz} in ferromagnets consists of two components [66],

$$\rho_{xz} = \rho_{xz}^N + \rho_{xz}^A = R_0 B + \mu_0 R_s M, \quad (2)$$

where the first term ρ_{xz}^N is the normal Hall resistivity contributed from the Lorentz force, and the second term ρ_{xz}^A is the AHE component. R_0 and R_s are ordinary and anomalous Hall coefficients, respectively. To extract the AHE component, the Hall resistivity was linearly fitted at high field (3 T to 7 T) to subtract ρ_{xz}^N , leaving ρ_{xz}^A , as shown in the inset of Fig. 5(a). The slope and y-axis intercept of the linear fit determine the R_0 and ρ_{xz}^A , respectively. The value of R_0 at 2 K is $0.32 \mu\Omega \text{ cm/T}$. The positive sign of the Hall coefficient indicates that the dominant carrier is hole type in CeGaSi. The carrier concentration n is estimated to be $\sim 1.9 \times 10^{21} \text{ cm}^{-3}$ according to the relation $R_0 \sim 1/|e|n$, and the mobility equals $16 \text{ cm}^2/\text{Vs}$ employing the formula $\mu = 1/(en\rho_{0T})$. The temperature dependence of them is shown in the inset of Fig. 5(b). Interestingly, the changes of carrier concentration and mobility both happen at 20 K rather than T_N , suggesting that the magnetic interactions are formed at 20 K and the effects on band structures are generated. Correspondingly, the transitions of the concentration and mobility are induced. The anomalous Hall coefficient R_s characterized as the magnitude of AHE can be extracted

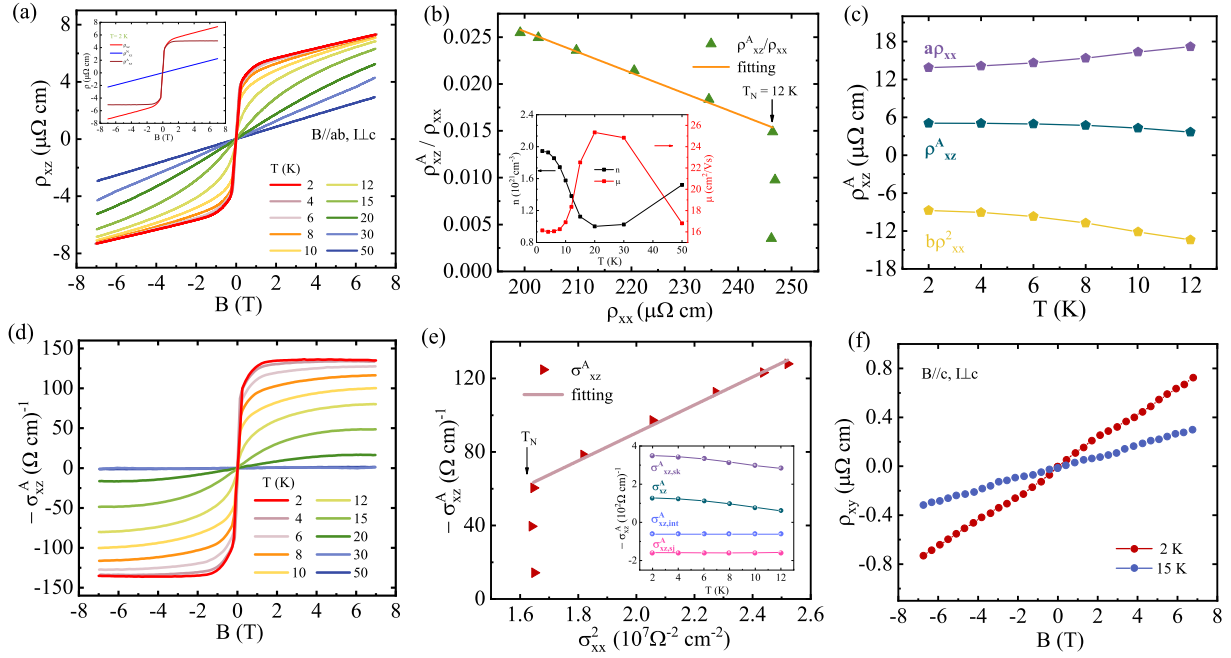


FIG. 5. (a) Field-dependent Hall resistivity curves at different temperature. Inset: The ρ_{xz} is decomposed into a normal and an anomalous part at 2 K. (b) Fitting of the ratio of anomalous Hall resistivity to longitudinal resistivity (ρ_{xz}^A/ρ_{xx}) versus ρ_{xx} curve at the temperature range of 2–12 K. Inset: Temperature dependence of the carrier concentration n and mobility μ . (c) Different contributions in ρ_{xz}^A with temperature are plotted on the same scale. (d) Field-dependent Hall conductivity $-\sigma_{xz}^A$. (e) Linear fitting of anomalous Hall conductivity $-\sigma_{xz}^A$ versus σ_{xx}^2 curve. Inset: $-\sigma_{xz}^A$ as a function of temperature. (f) The Hall resistivity of CeGaSi with the magnetic field applied along the c axis.

by $\rho_{xz}^A = R_s \mu_0 M$, in which M is taken from the intercept of the linear fit of $M(H)$ curves from 3 T to 7 T. Furthermore, R_s reaches a minimum value $3.84 \mu\Omega \text{ cm}/\text{T}$ at 2 K, which is still one order of magnitude larger than R_0 , indicating that the normal Hall effect is negligible compared to AHE in CeGaSi.

In general, there exist three kinds of mechanisms contributing to the origin of AHE: skew scattering, side jump, and intrinsic Berry curvature [9,21–23]. For the skew scattering the anomalous Hall resistivity should be proportional to the longitudinal resistivity [$\rho_{xz}^A \propto \rho_{xx}$ or $n = 1$ in $\rho_H/B = f(\rho_{xx}^n M/B)$], while the side jump and the intrinsic mechanism show the same relationship between anomalous Hall resistivity and the longitudinal resistivity ($\rho_{xz}^A \propto \rho_{xx}^2$ or $n = 2$ in $\rho_H/B = f(\rho_{xx}^n M/B)$) [67,68]). In fact, the mechanism of AHE in real material would arise from the interplay of multiple mechanisms and requires further research. In order to understand the mechanism of AHE in CeGaSi, the ρ_{xz}^A/ρ_{xx} versus ρ_{xx} curve is fitted by the following relation,

$$\rho_{xz}^A/\rho_{xx} = a + b\rho_{xx}, \quad (3)$$

where the parameters a and b contain information about skew scattering and both side-jump and intrinsic contribution, respectively. The fitting results are shown in Fig. 5(b), in which the skew scattering term ($a\rho_{xx}$) and side-jump plus intrinsic term ($b\rho_{xx}^2$) are obtained. The values are plotted in the same scale in Fig. 5(c). Therefore, the skew scattering mechanism is dominant in CeGaSi, while the side-jump and intrinsic mechanism also play an important role, which cannot be completely ignored in CeGaSi.

The anomalous Hall conductivity (AHC) σ_{xz}^A can be calculated from ρ_{xz}^A and ρ_{xx} through the relation

$$\sigma_{xz}^A = \frac{-\rho_{xz}^A}{\rho_{xx}^2 + \rho_{xz}^2}. \quad (4)$$

The field-dependent AHC for each temperature is displayed in Fig. 5(d) and the temperature-dependent AHC (σ_{xz}^A at $B = 0$) is plotted in the inset of Fig. 5(e), which reaches the maximum value $128 \Omega^{-1} \text{ cm}^{-1}$ at 2 K and disappears above 20 K. In order to extract the contribution of the intrinsic mechanism, the AHC can be further analyzed by the scaling behavior,

$$-\sigma_{xz}^A = (\alpha\sigma_{xx0}^{-1} + \beta\sigma_{xx0}^{-2})\sigma_{xx}^2 + m, \quad (5)$$

where α is the skew constant, σ_{xx0} is the residual conductivity at 2 K, and m is the intrinsic AHC [69]. The $-\sigma_{xz}^A$ versus σ_{xx}^2 along with the fit to Eq. (5) are shown in Fig. 5(e). From the fitting, the component of skew scattering plus side jump are attained with the positive value of $192 \Omega^{-1} \text{ cm}^{-1}$, and the intrinsic component is obtained with the negative value of $m = -62 \Omega^{-1} \text{ cm}^{-1}$, indicating that the intrinsic contribution is opposite to extrinsic ones. Combined with fitting results in resistivity as analyzed above, three individual values $\sigma_{xz,sk}^A \sim 350 \Omega^{-1} \text{ cm}^{-1}$, $\sigma_{xz,sj}^A \sim -158 \Omega^{-1} \text{ cm}^{-1}$, and $\sigma_{xz,int}^A \sim -62 \Omega^{-1} \text{ cm}^{-1}$ are roughly separated, as suggested in previous literature [69,70]. By comparing the magnitude, this points to the conclusion that the mechanism of AHE in CeGaSi is primarily governed by skew scattering, while the contribution of the side-jump and intrinsic mechanism cannot be ignored. This conclusion is consistent with that obtained from the analysis of anomalous Hall resistivity.

The field-dependent Hall measurement with $B \parallel c, I \perp c$ is also conducted and displayed in Fig. 5(f). Different from the case with $B \parallel ab, I \perp c$, a weak normal Hall effect is observed at 2 K (below T_N) and 15 K (above T_N) [61,71,72]. The carrier concentration and mobility at 2 K are $5.8 \times 10^{21} \text{ cm}^{-3}$ and $4.1 \text{ cm}^2/\text{Vs}$. The anisotropy of skew scattering and Berry curvature may result in the disappearance of AHE in this direction. On one hand, the skew scattering is an anisotropic scattering when the conducting electrons are passing through imperfections of the lattice, which may contribute to a smaller value or even leads to the absence of AHE in different directions. On the other hand, the AHC induced by the Berry curvature in CeGaSi may be anisotropic along different lattice axes, which may contribute to the opposite sign and equivalent values of AHC with that of extrinsic mechanism, ultimately leading to the cancellation of AHC. The anisotropic magnetoresistance and Hall resistivity establish the material CeGaSi as an interesting platform to study the novel magnetic and magnetotransport properties.

IV. CONCLUSIONS

In summary, we systematically investigated the magnetic and electrical transport properties of the AFM material CeGaSi with LaPtSi-type structure (space group $I4_1md$).

Specific heat measurements indicate a doublet ground state due to the crystalline electric field. The magnetic measurements on CeGaSi present the magnetic anisotropy, which orders ferromagnetically within the ab plane and antiferromagnetically along the c axis. The initially negative MR at low temperature with $B \parallel ab$ changes sign and becomes positive with further increasing B as it reaches the saturation. When the field is applied along the c axis, the MR remains negative, as a result of the suppression of spin scattering in the antiferromagnetic state. It is noteworthy that the prominent AHE is observed with $B \parallel ab$, which is mainly attributed to the contribution of skew scattering. Meanwhile, the AHE is absent with the field applied along the c axis. The MR and Hall measurements in two directions both indicate the anisotropic magnetotransport properties. Further theoretic calculations and neutron diffraction experiments will be useful to fully map out the detailed magnetic structure of CeGaSi and comprehend the mechanism of AHE in this fascinating compound.

ACKNOWLEDGMENT

This work is supported by the National Natural Science Foundation of China (Grant No. 12074425) and the National Key R&D Program of China (Grant No. 2019YFA0308602).

-
- [1] E. H. Hall, *Philos. Mag.* **10**, 301 (1880).
 [2] E. H. Hall, *Philos. Mag.* **12**, 157 (1881).
 [3] C. L. Chien and C. R. Westgate, *The Hall Effect and Its Applications* (Plenum, New York, 1980).
 [4] B. G. Park, J. Wunderlich, X. Martí, V. Holý, Y. Kurosaki, M. Yamada, H. Yamamoto, A. Nishide, J. Hayakawa, H. Takahashi *et al.*, *Nat. Mater.* **10**, 347 (2011).
 [5] E. Gomonay and V. Loktev, *Low Temp. Phys.* **40**, 17 (2014).
 [6] X. Martí, I. Fina, C. Frontera, J. Liu, P. Wadley, Q. He, R. Paull, J. Clarkson, J. Kudrnovský, I. Turek *et al.*, *Nat. Mater.* **13**, 367 (2014).
 [7] T. Jungwirth, X. Martí, P. Wadley, and J. Wunderlich, *Nat. Nanotechnol.* **11**, 231 (2016).
 [8] N. Nagaosa, J. Sinova, S. Onoda, A. H. MacDonald, and N. P. Ong, *Rev. Mod. Phys.* **82**, 1539 (2010).
 [9] R. Karplus and J. Luttinger, *Phys. Rev.* **95**, 1154 (1954).
 [10] J. Luttinger, *Phys. Rev.* **112**, 739 (1958).
 [11] E. Roman, Y. Mokrousov, and I. Souza, *Phys. Rev. Lett.* **103**, 097203 (2009).
 [12] D. Xiao, M.-C. Chang, and Q. Niu, *Rev. Mod. Phys.* **82**, 1959 (2010).
 [13] J. Weischenberg, F. Freimuth, J. Sinova, S. Blügel, and Y. Mokrousov, *Phys. Rev. Lett.* **107**, 106601 (2011).
 [14] K. Meng, J. Miao, X. Xu, J. Zhao, and Y. Jiang, *Phys. Lett. A* **381**, 1202 (2017).
 [15] I. Belopolski, K. Manna, D. S. Sanchez, G. Chang, B. Ernst, J. Yin, S. S. Zhang, T. Cochran, N. Shumiya, H. Zheng *et al.*, *Science* **365**, 1278 (2019).
 [16] E. Liu, Y. Sun, N. Kumar, L. Muechler, A. Sun, L. Jiao, S.-Y. Yang, D. Liu, A. Liang, Q. Xu *et al.*, *Nat. Phys.* **14**, 1125 (2018).
 [17] Q. Wang, Y. Xu, R. Lou, Z. Liu, M. Li, Y. Huang, D. Shen, H. Weng, S. Wang, and H. Lei, *Nat. Commun.* **9**, 3681 (2018).
 [18] Y. Wang, C. Xian, J. Wang, B. Liu, L. Ling, L. Zhang, L. Cao, Z. Qu, and Y. Xiong, *Phys. Rev. B* **96**, 134428 (2017).
 [19] K. Kim, J. Seo, E. Lee, K.-T. Ko, B. Kim, B. G. Jang, J. M. Ok, J. Lee, Y. J. Jo, W. Kang *et al.*, *Nat. Mater.* **17**, 794 (2018).
 [20] Q. Wang, S. Sun, X. Zhang, F. Pang, H. Lei *et al.*, *Phys. Rev. B* **94**, 075135 (2016).
 [21] J. Smit, *Physica* **21**, 877 (1955).
 [22] J. Smit, *Physica* **24**, 39 (1958).
 [23] L. Berger, *Phys. Rev. B* **2**, 4559 (1970).
 [24] S.-Y. Yang, Y. Wang, B. R. Ortiz, D. Liu, J. Gayles, E. Derunova, R. Gonzalez-Hernandez, L. Šmejkal, Y. Chen, S. S. Parkin *et al.*, *Sci. Adv.* **6**, eabb6003 (2020).
 [25] Y. Liu, C. Petrovic *et al.*, *Phys. Rev. B* **98**, 195122 (2018).
 [26] Z. Z. Jiang, X. Luo, J. Yan, J. J. Gao, W. Wang, G. C. Zhao, Y. Sun, J. G. Si, W. J. Lu, P. Tong, X. B. Zhu, W. H. Song, and Y. P. Sun, *Phys. Rev. B* **102**, 144433 (2020).
 [27] Y. Liu, H. Tan, Z. Hu, B. Yan, C. Petrovic *et al.*, *Phys. Rev. B* **103**, 045106 (2021).
 [28] M. Lyu, J. Xiang, Z. Mi, H. Zhao, Z. Wang, E. Liu, G. Chen, Z. Ren, G. Li, and P. Sun, *Phys. Rev. B* **102**, 085143 (2020).
 [29] H.-Y. Yang, B. Singh, B. Lu, C.-Y. Huang, F. Bahrami, W.-C. Chiu, D. Graf, S.-M. Huang, B. Wang, H. Lin *et al.*, *APL Mater.* **8**, 011111 (2020).
 [30] H.-Y. Yang, B. Singh, J. Gaudet, B. Lu, C.-Y. Huang, W.-C. Chiu, S.-M. Huang, B. Wang, F. Bahrami, B. Xu *et al.*, *Phys. Rev. B* **103**, 115143 (2021).
 [31] M. S. Alam, A. Fakhredine, M. Ahmad, P. K. Tanwar, H.-Y. Yang, F. Tafti, G. Cuono, R. Islam, B. Singh, A. Lynnyk, C. Autieri, and M. Matusiak, *Phys. Rev. B* **107**, 085102 (2023).

- [32] E. Cheng, L. Yan, X. Shi, R. Lou, A. Fedorov, M. Behnami, J. Yuan, Y. Xu, Y. Xu, W. Xia *et al.*, [arXiv:2301.03800](#).
- [33] H. Su, X. Shi, J. Yuan, Y. Wan, E. Cheng, C. Xi, L. Pi, X. Wang, Z. Zou, N. Yu *et al.*, *Phys. Rev. B* **103**, 165128 (2021).
- [34] M. M. Piva, J. C. Souza, V. Brousseau-Couture, S. Sorn, K. R. Pakuszewski, J. K. John, C. Adriano, M. Côté, P. G. Pagliuso, A. Paramekanti, and M. Nicklas, *Phys. Rev. Res.* **5**, 013068 (2023).
- [35] J.-F. Wang, Q.-X. Dong, Z.-P. Guo, M. Lv, Y.-F. Huang, J.-S. Xiang, Z.-A. Ren, Z.-J. Wang, P.-J. Sun, G. Li *et al.*, *Phys. Rev. B* **105**, 144435 (2022).
- [36] J. Gaudet, H.-Y. Yang, S. Baidya, B. Lu, G. Xu, Y. Zhao, J. A. Rodriguez-Rivera, C. M. Hoffmann, D. E. Graf, D. H. Torchinsky *et al.*, *Nat. Mater.* **20**, 1650 (2021).
- [37] M. Lyu, Z. Wang, K. Ramesh Kumar, H. Zhao, J. Xiang, and P. Sun, *J. Appl. Phys.* **127**, 193903 (2020).
- [38] W. Cao, Y. Su, Q. Wang, C. Pei, L. Gao, Y. Zhao, C. Li, N. Yu, J. Wang, Z. Liu *et al.*, *Chin. Phys. Lett.* **39**, 047501 (2022).
- [39] X. Yao, J. Gaudet, R. Verma, D. E. Graf, H.-Y. Yang, F. Bahrami, R. Zhang, A. A. Aczel, S. Subedi, D. H. Torchinsky *et al.*, *Phys. Rev. X* **13**, 011035 (2023).
- [40] J.-F. Wang, Q.-X. Dong, Y.-F. Huang, Z.-S. Wang, Z.-P. Guo, Z.-J. Wang, Z.-A. Ren, G. Li, P.-J. Sun, X. Dai *et al.*, *Phys. Rev. B* **108**, 024423 (2023).
- [41] N. Zhang, X. Ding, F. Zhan, H. Li, H. Li, K. Tang, Y. Qian, S. Pan, X. Xiao, J. Zhang *et al.*, *Phys. Rev. Res.* **5**, L022013 (2023).
- [42] S.-i. Kashiba, S. Maekawa, S. Takahashi, and M. Tachiki, *J. Phys. Soc. Jpn.* **55**, 1341 (1986).
- [43] K. Synoradzki, P. Skokowski, M. Koterlyn, J. Sebesta, D. Legut, T. Toliński *et al.*, *J. Magn. Magn. Mater.* **547**, 168833 (2022).
- [44] E. S. R. Gopal, *Specific Heats at Low Temperatures* (Plenum, New York, 1966).
- [45] C. Kittel, *Introduction to Solid State Physics* (Wiley & Sons, New York, 1976).
- [46] V. Anand and D. C. Johnston, *J. Phys.: Condens. Matter* **26**, 286002 (2014).
- [47] G. Dwari, S. Sasmal, S. Dan, B. Maity, V. Saini, R. Kulkarni, S. Banik, R. Verma, B. Singh, and A. Thamizhavel, *Phys. Rev. B* **107**, 235117 (2023).
- [48] L. Roeland, G. Cock, F. Muller, A. Moleman, K. McEwen, R. Jordan, and D. Jones, *J. Phys. F: Metal Phys.* **5**, L233 (1975).
- [49] J. Szade, *J. Less Common. Met.* **136**, 101 (1987).
- [50] E. Bauer and M. Rotter, *Properties and Applications of Complex Intermetallics* (World Scientific, Singapore, 2010), pp. 183–248.
- [51] A. B. Pippard, *Magnetoresistance in Metals* (Cambridge University Press, Cambridge, UK, 1989), Vol. 2.
- [52] X. Huang, L. Zhao, Y. Long, P. Wang, D. Chen, Z. Yang, H. Liang, M. Xue, H. Weng, Z. Fang *et al.*, *Phys. Rev. X* **5**, 031023 (2015).
- [53] F. Arnold, C. Shekhar, S.-C. Wu, Y. Sun, R. D. Dos Reis, N. Kumar, M. Naumann, M. O. Ajeesh, M. Schmidt, A. G. Grushin *et al.*, *Nat. Commun.* **7**, 11615 (2016).
- [54] C.-L. Zhang, S.-Y. Xu, I. Belopolski, Z. Yuan, Z. Lin, B. Tong, G. Bian, N. Alidoust, C.-C. Lee, S.-M. Huang, T.-R. Chang, G. Chang, C.-H. Hsu, H.-T. Jeng, M. Neupane, D. S. Sanchez, H. Zheng, J. Wang, H. Lin, C. Zhang, H.-Z. Lu, S.-Q. Shen, T. Neupert, M. Zahid Hasan, and S. Jia, *Nat. Commun.* **7**, 10735 (2016).
- [55] B. Raquet, M. Viret, E. Sondergard, O. Cespedes, and R. Mamy, *Phys. Rev. B* **66**, 024433 (2002).
- [56] A. Mihai, J. Atané, A. Marty, P. Warin, and Y. Samson, *Phys. Rev. B* **77**, 060401(R) (2008).
- [57] D. G. Oh, J. H. Kim, M. K. Kim, K. W. Jeong, H. J. Shin, J. M. Hong, J. S. Kim, K. Moon, N. Lee, and Y. J. Choi, *Sci. Rep.* **13**, 3391 (2023).
- [58] S. Blundell, *Magnetism in Condensed Matter* (Oxford University Press, New York, 2001).
- [59] H. Yamada and S. Takada, *J. Phys. Soc. Jpn.* **34**, 51 (1973).
- [60] D. Ram, S. Malick, Z. Hossain, and D. Kaczorowski, *Phys. Rev. B* **108**, 024428 (2023).
- [61] B. Meng, H. Wu, Y. Qiu, C. Wang, Y. Liu, Z. Xia, S. Yuan, H. Chang, and Z. Tian, *APL Mater.* **7**, 051110 (2019).
- [62] W. Zhuo, B. Lei, S. Wu, F. Yu, C. Zhu, J. Cui, Z. Sun, D. Ma, M. Shi, H. Wang *et al.*, *Adv. Mater.* **33**, 2008586 (2021).
- [63] S. H. Lee, Y. Zhu, Y. Wang, L. Miao, T. Pillsbury, H. Yi, S. Kempinger, J. Hu, C. A. Heikes, P. Quarterman, W. Ratcliff, J. A. Borchers, H. Zhang, X. Ke, D. Graf, N. Alem, C. Z. Chang, N. Samarth, and Z. Mao, *Phys. Rev. Res.* **1**, 012011(R) (2019).
- [64] E. J. Telford, A. H. Dismukes, R. L. Dudley, R. A. Wiscons, K. Lee, D. G. Chica, M. E. Ziebel, M.-G. Han, J. Yu, S. Shabani *et al.*, *Nat. Mater.* **21**, 754 (2022).
- [65] J. Yuan, X. Shi, H. Su, X. Zhang, X. Wang, N. Yu, Z. Zou, W. Zhao, J. Liu, and Y. Guo, *Phys. Rev. B* **106**, 054411 (2022).
- [66] C. M. Hurd, *The Hall Effect in Metals and Alloys* (Plenum Press, New York, 1972).
- [67] V. V. Glushkov, I. I. Lobanova, V. Y. Ivanov, and S. V. Demishev, *JETP Lett.* **101**, 459 (2015).
- [68] V. V. Glushkov, I. I. Lobanova, V. Y. Ivanov, V. V. Voronov, V. A. Dyadkin, N. M. Chubova, S. V. Grigoriev, and S. V. Demishev, *Phys. Rev. Lett.* **115**, 256601 (2015).
- [69] Y. Tian, L. Ye, and X. Jin, *Phys. Rev. Lett.* **103**, 087206 (2009).
- [70] L. Wu, Y. Li, J. Xu, D. Hou, and X. Jin, *Phys. Rev. B* **87**, 155307 (2013).
- [71] H. Hodovanets, C. J. Eckberg, P. Y. Zavalij, H. Kim, W.-C. Lin, M. Zic, D. J. Campbell, J. S. Higgins, and J. Paglione, *Phys. Rev. B* **98**, 245132 (2018).
- [72] K. Cho, W. H. Shon, K. Kyoo, J. Bae, J. Lee, J. H. Yun, S. Yoon, B. Cho, P. Rawat, Y.-K. Kim *et al.*, *Mater. Today Commun.* **35**, 106411 (2023).